

A Methodology to Analyze Changes in Lipid Core and Calcification Onto Fibrous Cap Vulnerability: The Human Atherosclerotic Carotid Bifurcation as an Illustratory Example

Dimitrios E. Kiousis

Stephan F. Rubinigg

Institute of Biomechanics,
Center of Biomedical Engineering,
Graz University of Technology,
Kronsgasse 5-I,
8010 Graz, Austria

Martin Auer

Department of Solid Mechanics,
School of Engineering Sciences,
Royal Institute of Technology (KTH),
10044 Stockholm, Sweden

Gerhard A. Holzapfel¹

Institute of Biomechanics,
Center of Biomedical Engineering,
Graz University of Technology,
Kronsgasse 5-I,
8010 Graz, Austria;
Department of Solid Mechanics,
School of Engineering Sciences,
Royal Institute of Technology (KTH),
10044 Stockholm, Sweden
e-mail: holzapfel@tugraz.at

A lipid core that occupies a high proportion of the plaque volume in addition to a thin fibrous cap is a predominant indicator of plaque vulnerability. Nowadays, noninvasive imaging modalities can identify such structural components, however, morphological criteria alone cannot reliably identify high-risk plaques. Information, such as stresses in the lesion's components, seems to be essential. This work presents a methodology able to analyze the effect of changes in the lipid core and calcification on the wall stresses, in particular, on the fibrous cap vulnerability. Using high-resolution magnetic resonance imaging and histology of an ex vivo human atherosclerotic carotid bifurcation, a patient-specific three-dimensional geometric model, consisting of four tissue components, is generated. The adopted constitutive model accounts for the nonlinear and anisotropic tissue behavior incorporating the collagen fiber orientation by means of a novel and robust algorithm. The material parameters are identified from experimental data. A novel stress-based computational cap vulnerability index is proposed to assess quantitatively the rupture-risk of fibrous caps. Nonlinear finite element analyses identify that the highest stress regions are located at the vicinity of the shoulders of the fibrous cap and in the stiff calcified tissue. A parametric analysis reveals a positive correlation between the increase in lipid core portion and the mechanical stress in the fibrous cap and, hence, the risk for cap rupture. The highest values of the vulnerability index, which correlate to more vulnerable caps, are obtained for morphologies for which the lipid cores were severe; heavily loaded fibrous caps were thus detected. The proposed multidisciplinary methodology is able to investigate quantitatively the mechanical behavior of atherosclerotic plaques in patient-specific stenoses. The introduced vulnerability index may serve as a more quantitative tool for diagnosis, treatment and prevention.

[DOI: 10.1115/1.4000078]

Keywords: artery, calcification, carotid bifurcation, fibrous cap, lipid core, MRI, vulnerability

1 Introduction

Atherosclerosis is the main determinant of cardiovascular diseases, the leading cause of cardiovascular morbidity and mortality around the globe [1,2]. Although luminal narrowing and exaggerated or anomalous vasoconstriction contribute to some of the clinical manifestations of arterial diseases, it is the superimposition of an arterial thrombus over an underlying ruptured or eroded plaque that is responsible for the vast majority of acute ischemic syndromes such as myocardial infarction or cerebrovascular accident [3–5]. Cerebrovascular atherosclerosis, for example, is the result of half of the stroke events including carotid plaques; plaque rupture is a critical event in the evolution of atherosclerosis.

Hence, it is crucial to determine whether a plaque is vulnerable [6], and therefore life-threatening with the risk of stroke, or resistant and innocuous. The ability to identify rupture-prone high-risk plaques and to intervene successfully before acute plaque rupture occurs has been an elusive goal of clinicians over the past decades.

A series of postmortem observations in patients with acute ischemic syndromes revealed that predominant features of plaque vulnerability include increased numbers of macrophages, increased expression of tissue factor, reduced number of smooth muscle cells, a lipid core that occupies a high proportion of the overall plaque volume, and a thin fibrous cap (see, e.g., Refs. [6–9]). The rapid development in the area of arterial wall imaging made the detection of the lipid core and the fibrous cap feasible. A review of the invasive and noninvasive imaging modalities is given in Ref. [10]. High-resolution magnetic resonance imaging represents the best promise of in vivo quantitative characterization of plaque morphology [11–13], and appears to be a favorable

¹Corresponding author.

Contributed by the Bioengineering Division of ASME for publication in the JOURNAL OF BIOMECHANICAL ENGINEERING. Manuscript received August 25, 2008; final manuscript received February 19, 2009; accepted manuscript posted September 1, 2009; published online October 29, 2009. Editor: Michael Sacks.

assessment method of fibrous caps and a promising diagnostic strategy.

Plaque rupture is highly complex, multifactorial, and morphological criteria alone cannot reliably identify high-risk plaques. Early studies based on structural mechanics [14–16] identified a strong connection between plaque fracture and mechanical loading through blood pressure. It was especially shown that large eccentric lipid cores impose a mechanical disadvantage to the plaque by redistributing circumferential stress to the shoulders' regions of the plaques; hence, to the location where fibrous caps in most cases tend to rupture [17]. These investigations provided strong evidence that acute plaque fracture is linked to plaque composition and to high mechanical stresses, which exceed the ultimate tensile strength of the fibrous cap. Thus, it is now accepted that computational mechanics in addition to imaging is necessary for the assessment of the lesions' vulnerability.

Therefore, in recent years more attempts came from the biomechanics community by applying numerical tools in conjunction with imaging modalities, such as magnetic resonance imaging (MRI) and intravascular ultrasound (IVUS), to provide deeper insights into plaque fracture. Several studies support the interrelation between the tissue components' structure and material properties and the overall mechanical environment of the plaque, and especially the fibrous cap responsible for acute cardiovascular events. However, the majority of published efforts have utilized simplified modeling approaches based on two-dimensional model plaques or assumed plane-stress states [14–16,18–23]. The most promising approaches [24,25] have presented three-dimensional (3D) analyses of plaques based on fluid-structure interaction to identify flow and stress conditions and to computationally assess the fracture risk-factor of structurally different atherosclerotic lesions. In all mentioned studies, though, the arterial tissues were assumed to be isotropic, an assumption that does not reflect the experimentally observed anisotropic behavior of nondiseased [26,27] and diseased [28,29] vascular tissues. The aforementioned studies undoubtedly offer notable insights into the mechanics of plaque vulnerability. However, isotropic material models do not yield reliable quantitative results [30] and restrict the biomechanical interpretation of the findings significantly. Consequently, there is a need for modeling the complex 3D arterial structure, the tissue geometry, and the related mechanics in a more realistic way.

As requested by several studies, including the recent one by Beaussier et al. [31], the main objective of the present study is the development of a combined imaging and computational methodology able to analyze the effect of changes in the lipid core and calcification components on the 3D mechanical environment of an artery in general and on the fibrous cap vulnerability in particular. A human carotid bifurcation with high-grade atherosclerotic plaque serves as a pilot study *ex vivo* to show the power of the presented methodology. A patient-specific 3D geometric model is generated from high-resolution MRI, histological examination, and a non-uniform rational B-splines (NURBS) surface-fitting technique. The arterial wall is considered to be nonhomogeneous consisting of four different tissue components. The adopted constitutive model takes into account the nonlinearity and anisotropy of the fibrous cap and the portion of the nondiseased wall incorporating the collagen fiber orientation by using a novel algorithm. The material parameters are identified from novel experimental data of human carotid bifurcations and from the literature. Different lesion compositions lead to different stress patterns within the lesions, and certain types of plaques are more prone to stress concentrations and eventual rupture than others. For example, large lipid cores are the main determinant of high-risk lesions [6,32,33]. Hence, within the present study we investigate the effect of changes in lipid core and calcification on the stress distribution, especially in the fibrous cap, by keeping the cap thickness constant. In particular, we vary the volume ratio of lipid core and calcification in the generated morphological and computational

model. Finally, the different models are quantified using a vulnerability index with the potential to provide a quantitative assessment of cap vulnerability.

2 Biomechanical Arterial Model

In this section we describe the investigated specimen, the employed imaging technique, the segmentation and the generation of the 3D geometry for the arterial wall. We proceed by introducing the constitutive model and the performed mechanical tests to identify the material parameters.

2.1 Specimen. One carotid bifurcation was excised from a human cadaver (male, 76 years) during autopsy, i.e., donor III in Ref. [34]. The artery had an atherosclerotic lesion of type V, according to the classification proposed in Ref. [35]. A type V lesion may consist of multiple layers of alternating composition—two or more lipid cores of unequal size, separated from each other by unequal layers of reparative fibromuscular tissue, and irregularly stacked one on top of the other. After harvesting, the specimen was stored in a 37°C calcium-free 0.9% NaCl physiological saline solution (PSS) at 4°C (approximately 4–8 h) until magnetic resonance scanning. Use of autopsy material from the human subject was approved by the Ethics Committee, Medical University Graz, Austria.

2.2 Magnetic Resonance Imaging, Geometric Model. To identify the 3D geometry of the vessel, high-resolution MRI was used. The artery was scanned on a whole-body MR system at 1.5 T (Philips ACS-NT). Three-dimensional turbo spin echo sequences were applied to achieve high spatial resolution and a sufficient signal-to-noise ratio in an acceptable scan time of 10–15 min. We obtained 45 MRI sections with a slice thickness of 0.8 mm and an in plane resolution of 0.15 mm. Three representative T1-weighted MR images of the carotid bifurcation are shown in Fig. 1.

Subsequently, we applied an automatic segmentation method with active contours based on a generalized gradient vector flow [36]. With this method we segmented three tissue components: (i) nondiseased wall W-nos,² (ii) calcification I-c, (iii) lipid core I-lp [30]. The fibrous cap I-fc (fibrotic part at the luminal border) was segmented manually by a pathologist using several histological sections. Finally, based on the segmented MR images, the components' boundaries were described by means of NURB control points [37], and the volumes of the arterial tissues were reconstructed using the commercial software RHINOCEROS [38]. The 3D geometric model with two characteristic cross sections are shown in Fig. 2.

2.3 Constitutive Model. Arterial walls are nonhomogeneous, anisotropic, highly deformable, nearly incompressible composites and exhibit a pseudoelastic response (see, e.g., Refs. [39–41]). The choice of the constitutive model to describe such a complex behavior is of fundamental importance for the reliable prediction of the stress environment and the assessment of plaque rupture. We adopt the constitutive model as presented in Refs. [27,42] and review it briefly here.

We postulate the existence of a strain-energy function Ψ and assume the decoupled form $\Psi = U(J) + \bar{\Psi}$, where $J = \det \mathbf{F} > 0$ is the volume ratio and \mathbf{F} is the deformation gradient. The strictly convex function U is responsible for the volumetric elastic response of the material, while the convex function $\bar{\Psi}$ takes care of the isochoric elastic response. Since we treat the individual tissue components like incompressible materials, U takes on the role of a (purely mathematically motivated) penalty function enforcing the incompressibility constraint. We have U chosen to be

²The abbreviation “nos” stands for not otherwise specified. In the context of the present study it means “no appreciable disease” or, more precisely, “nonatherosclerotic.”

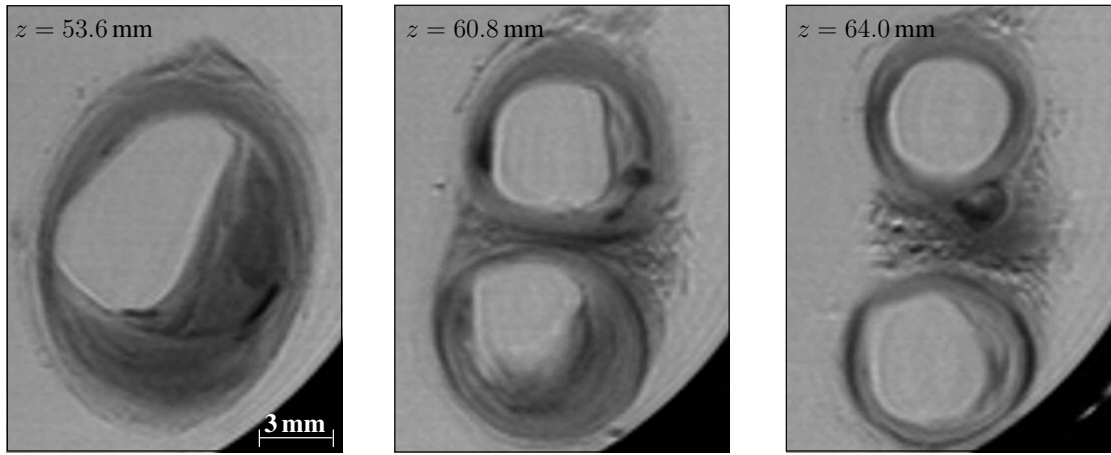


Fig. 1 Representative T1-weighted MR images (slice thickness of 0.8 mm and in plane resolution of 0.15 mm) showing different sections of the excised human carotid bifurcation, with z referring to the coordinate system, as introduced in Fig. 2

$$U(J) = \frac{\kappa}{2}(J-1)^2 \quad (1)$$

where κ is the bulk modulus, which serves as a user-specified (positive) penalty parameter. Clearly, with increasing κ the violation of the constraint is reduced. If the restriction on the value $\kappa \rightarrow \infty$ is taken, the constraint condition is exactly enforced, and then Ψ represents a functional for an incompressible material with $J=1$.

The two tissue components W-nos and I-fc are considered as composites reinforced by two families of (collagen) fibers embedded in a noncollagenous groundmatrix assumed to be isotropic. An additive split of the isochoric strain-energy function $\bar{\Psi}$ into an isotropic function $\bar{\Psi}_g$, associated with the noncollagenous groundmatrix, and two anisotropic functions, $\bar{\Psi}_{f,i}$, $i=1,2$, are used as in Refs. [43,44]; thus, $\bar{\Psi}$ may be written as

$$\bar{\Psi} = \bar{\Psi}_g + \sum_{i=1,2} \bar{\Psi}_{f,i} \quad (2)$$

Following Refs. [45,46], the noncollagenous groundmatrix is modeled as an isotropic neo-Hookean material, i.e.,

$$\bar{\Psi}_g(\bar{\mathbf{C}}) = \frac{\mu}{2}(\bar{I}_1 - 3) \quad (3)$$

where μ is a material parameter, and $\bar{I}_1 = \text{tr} \bar{\mathbf{C}}$ is the first invariant of the modified Cauchy–Green tensor $\bar{\mathbf{C}} = J^{-2/3} \mathbf{F}^T \mathbf{F}$ [47]. Following Refs. [27,42], the second term in Eq. (2) has the form

$$\bar{\Psi}_{f,i}(\bar{I}_{4,i}) = \frac{k_1}{2k_2} \{ \exp[k_2[(1-\rho)(\bar{I}_1 - 3)^2 + \rho(\bar{I}_{4,i} - 1)^2]] - 1 \} \quad (4)$$

$i = 1, 2$

where k_1 and k_2 are positive material parameters, and $\bar{I}_{4,i}$ are modified invariants defined as $\bar{I}_{4,1} = \mathbf{M} \otimes \mathbf{M}$ and $\bar{I}_{4,2} = \mathbf{M}' \otimes \mathbf{M}'$, where \mathbf{M} and \mathbf{M}' denote vectors, which point in the mean (reference) direction of the two families of collagen fibers. The scalar parameter $\rho \in [0, 1]$ can be interpreted as a weighting factor that allows the characterization of a state between isotropic response (equally distributed collagen fibers) and anisotropic response (ideal alignment of collagen fibers). Hence, for $\rho=1$, Eq. (4) reduces to

$$\bar{\Psi}_{f,i}(\bar{I}_{4,i}) = \frac{k_1}{2k_2} \{ \exp[k_2(\bar{I}_{4,i} - 1)^2] - 1 \}, \quad i = 1, 2 \quad (5)$$

which is according to Refs. [43,48], while for $\rho=0$, Eq. (4) becomes

$$\bar{\Psi}_f(\bar{I}_1) = \frac{k_1}{2k_2} \{ \exp[k_2(\bar{I}_1 - 3)^2] - 1 \} \quad (6)$$

which is similar to the function proposed in Ref. [49] (100% isotropic distribution). Hence, ρ can be seen as a “switch” parameter between isotropy and anisotropy describing the “degree of anisotropy” of the tissue.

The remaining tissue components I-c and I-lp are considered as isotropic materials described by a strain-energy function, which is the sum of the functions (1) and (3).

2.4 Mechanical Tests, Related Material Parameters. In order to determine the parameters of functions (3) and (4), we per-

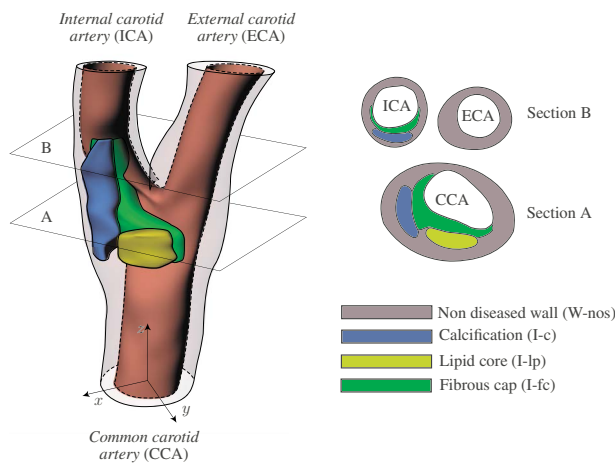


Fig. 2 3D geometric model of a stenotic human carotid bifurcation (atherosclerotic lesion of type V [35]) based on in vitro MRI (Fig. 1) reconstructed using NURBS. Four arterial tissues are considered: nondiseased wall (W-nos), calcification (I-c), lipid core (I-lp), and fibrous cap (I-fc). Two characteristic cross sections are shown at axial planes $z=53.6$ mm (Section A) and $z=64.0$ mm (Section B).

Table 1 Material parameters for nondiseased wall (W-nos), fibrous cap (I-fc), calcification (I-c), and lipid core (I-lp)

| Tissue | Material parameters | | | | |
|-------------|---------------------|----------------|-------|--------------------|--------|
| | μ (kPa) | k_1 (kPa) | k_2 | φ (deg) | ρ |
| W-nos, I-fc | 43.78 | 93.63 | 79.57 | 17.22 | 0.70 |
| I-c | 4.50×10^3 | - | - | - | - |
| I-lp | 0.10 | - | - | - | - |

formed extension-inflation tests on the described human carotid artery at different axial stretches. The load was applied quasistatically, while the transmural pressure, axial force, outer diameter, and gauge length of the arterial specimen were continuously recorded. Details on the experimental setup and the experimental procedure are provided in Refs. [26,34].

We use here experimental data obtained from the related internal carotid artery. The material parameters for W-nos were determined by fitting Eqs. (3) and (4) to the data using a least-squares algorithm. We assumed that the collagenous components of the tissues were symmetrically disposed with respect to the vertical axis (orthotropic behavior). We neglected the radial component of the vectors \mathbf{M} and \mathbf{M}' thus allowing the definition of the mean directions by the single parameter φ , which denotes the angle between the mean collagen fiber directions and the circumferential direction of the artery.

Material parameters for I-fc were assumed to be the same as for W-nos, while the parameters for the calcification I-c were adopted from Ref. [29]. Therein it was shown that I-c exhibits very stiff and linear mechanical responses with an average Young's modulus of 12.6 MPa. By assuming a nearly incompressible response we obtain the value $\mu=4.50$ MPa, which enters function (3). The lipid core I-lp is a relatively soft material when compared with other tissues of an atherosclerotic artery. It was modeled as a nearly incompressible neo-Hookean material with a comparatively low shear modulus. The value was taken from Ref. [30] to be $\mu=0.1$ kPa; the same approach was pursued in Refs. [42,50]. The material parameters for the individual tissues are summarized in Table 1. The ratios of the (penalty) parameters κ , as in Eq. (1), to

the moduli μ for the arterial components were chosen to be roughly equivalent to two to three orders of magnitude.

3 Computational Model

This section outlines a novel algorithm to generate the collagen fiber directions in arterial walls. It describes the finite element model including the generation of the mesh and the boundary and loading conditions. Next, four models are introduced by varying the volumes of two tissue components. These models serve as a basis for the biomechanical investigation of the relationship between tissue composition and vulnerability. Finally, a (scalar) computational vulnerability index is introduced to assess the rupture-risk of the fibrous cap.

3.1 Definition of the Fiber Directions. The anisotropic constitutive model (4) requires the mean preferred directions \mathbf{M} and \mathbf{M}' of the collagen fibers in the undeformed configuration as input data. This, however, is not a trivial task when realistic arterial geometries are considered, as in the present study. The complex and irregular patient-specific models hinder a straightforward description of the local material axes. Therefore, special numerical strategies are required.

The aim is to identify the fiber directions \mathbf{M} and \mathbf{M}' at a typical point \mathbf{P} in the tissue. Thereby the angle φ between the collagen fibers (considered arranged in symmetrical spirals) and the circumferential direction is assumed to be known (Table 1). The algorithm used to generate the collagen fabric in space is based on tangential planes. Figures 3(a) and 3(b) show the respective transverse and longitudinal sections of the bifurcation model in addition to two planes Ω_1 and Ω_2 , which represent the tangential planes. The corresponding normal vectors at the projections of the point \mathbf{P} on Ω_1 and Ω_2 are denoted by \mathbf{N}_1 and \mathbf{N}_2 , respectively. The vector product $\mathbf{N}_2 \times \mathbf{N}_1$ yields the projected fiber vectors $\bar{\mathbf{M}} = -\bar{\mathbf{M}}'$, which are located on the intersection $\Omega_1 \cap \Omega_2$ of the tangential plane (Fig. 3(a)). Finally, the fiber vectors \mathbf{M} and \mathbf{M}' can easily be computed as

$$\mathbf{M} = \cos\varphi \bar{\mathbf{M}} - \sin\varphi \bar{\mathbf{N}}_1, \quad \mathbf{M}' = \cos\varphi \bar{\mathbf{M}}' - \sin\varphi \bar{\mathbf{N}}_1 \quad (7)$$

where $\bar{\mathbf{N}}_1$ is the projection of the normal vector \mathbf{N}_1 on the plane Ω_2 , as shown in Fig. 3(b).

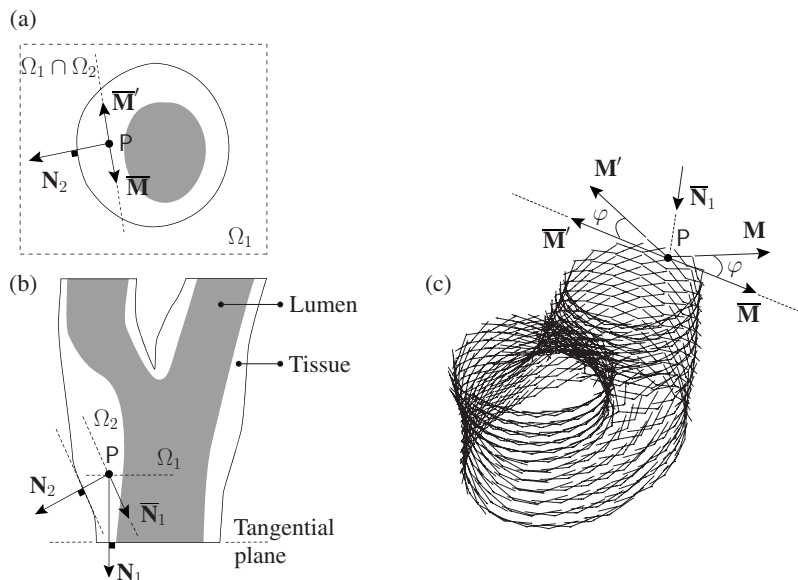


Fig. 3 Transverse (a) and longitudinal (b) sections of the carotid bifurcation model. Every point \mathbf{P} is projected onto its corresponding tangential planes Ω_1 and Ω_2 . 3D view of the computed fiber direction vectors \mathbf{M} and \mathbf{M}' at the center of the superficial finite elements of the carotid bifurcation wall (c).

The methodology outlined above was applied to the carotid bifurcation in question. The fiber directions were computed at the center of each finite element with the angle φ , as given in Table 1. Figure 3(c) shows the 3D fiber structure of the carotid bifurcation wall represented by vectors \mathbf{M} and \mathbf{M}' for a portion close to the bifurcation. For reasons of clarity, only the direction vectors at the center of the superficial finite elements are plotted. The advantage of the described method is its simplicity in terms of conception and implementation. As it can be seen in Fig. 3(c), the proposed strategy has the ability to provide solutions for large arbitrarily curved patient-specific 3D models.

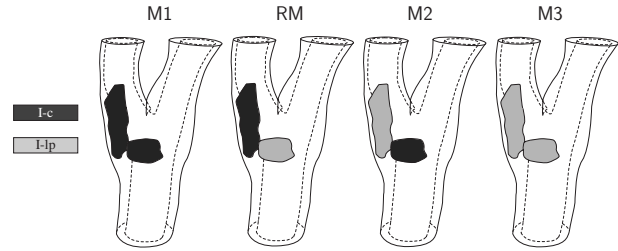
3.2 Finite Element Model. The 3D geometric model of the carotid bifurcation wall, as shown in Fig. 2, was generated using the commercially available CUBIT Geometry and Mesh Generation Toolkit [51]. The finite element mesh was generated with matching nodes on the four tissue interfaces, and no algorithmic treatment was required to link them. The mesh consists of approximately 7000 eight-node isoparametric hexahedral elements, which are based on a three-field Hu-Washizu variational formulation [47]. The used mixed $Q1/P0$ -elements, as implemented in the multipurpose finite element analysis program FEAP [52], provide an efficient and proper description of the isochoric deformation of the tissue components.

Experimental investigations (see, e.g., Refs. [27,28,53,54]) show that human vessels exhibit an axial in situ prestretch. In contrast to healthy arteries, highly stenotic human vessels (as the one investigated here) show a relatively small prestretch, for example, a value of 1.03 is reported in Ref. [28], while an average value of 1.044 is documented in Ref. [27]. In the present study a displacement-controlled axial stretch of $\lambda_z=1.05$ was initially applied to all nodes located at the upper face of the arterial wall. Subsequently, all nodes of the upper and lower faces (cross sections at the inlet and outlet) of the bifurcation were fixed in all three directions. Next, a blood pressure of 140 mmHg was applied which was performed by follower (deformation-dependent) pressure loads applied to each facet of the luminal surface.

3.3 Model Variation. The quantitative effect of the severity of lipid core I-lp and calcification I-c on the mechanical stress environment and eventually on the stability of the considered carotid bifurcation is studied. Detailed analyses are performed in which the volumes V_{I-lp} and V_{I-c} (in percentage) of the respective tissue components serve as parameters. We generate and analyze variations on the acquired reference model (shown in Fig. 2) by keeping the cap thickness unchanged. The geometry, as shown in Fig. 2, remains the same in *all* variations. However, the material models and parameters of the plaque forming tissues (I-lp and I-c) are interchanged or completely substituted by each other. This is shown in Table 2, where the black region represents the calcification (I-c) and the light-gray region the lipid core (I-lp). In the reference model, which we subsequently call the reference model (RM), the I-lp volume comprises 25% of the volume of the plaque, while the I-c volume comprises the remaining 75%. A first variation in RM is model M1 in which I-lp is completely substituted by I-c ($V_{I-c}=100\%$). Model M2 has the ratio $V_{I-lp}=75\%$, $V_{I-c}=25\%$ of the two involved tissues, while in model M3 I-c is not present ($V_{I-lp}=100\%$). Hence, the volumes of I-lp in models M1, RM, M2, and M3 vary from 0% to 100%. Table 2 summarizes the four investigated models.

3.4 Index of Cap Vulnerability. Here we introduce scalar quantities to serve as vulnerability criteria. The idea to use such indicators goes back to the studies [42,55,50], which aim to identify plaque risk and assess stent design. We propose a novel (computational) vulnerability index, subsequently denoted as ξ , to quantify the loaded fibrous cap I-fc. Thus,

Table 2 Four models characterized by variations of the volume V_{I-lp} (in %) of the lipid core and the volume V_{I-c} of the calcification. Model RM refers to the reference model according to Fig. 2.



| Model | Description | Tissue volume in % | |
|-------|------------------------------|--------------------|-----------|
| | | V_{I-lp} | V_{I-c} |
| M1 | I-lp modeled as I-c | 0 | 100 |
| RM | Reference model (Fig. 2) | 25 | 75 |
| M2 | Interchange of I-lp with I-c | 75 | 25 |
| M3 | I-c modeled as I-lp | 100 | 0 |

$$\xi = w_1 D_1 + w_2 D_2 \quad (8)$$

where ξ is a function of the user-defined parameters $w_1, w_2 \in [0, 1]$, which are weighting factors with the condition $w_1 + w_2 = 1$, while D_1 and D_2 are stress-dependent scalars subsequently explained.

The scalar D_1 is defined as

$$D_1 = \frac{\max(\sigma^{I-fc})}{\sigma_{allow}}, \quad \sigma_{allow} = \frac{\sigma_{ult}^{I-fc}}{f_s} \quad (9)$$

where $\max(\sigma^{I-fc})$ denotes the maximum principal Cauchy stress in I-fc, and σ_{allow} denotes an allowable stress that must not exceeded anywhere in the structure of I-fc. In addition, we have introduced the notation f_s for the factor of safety with respect to the ultimate stress σ_{ult}^{I-fc} of I-fc in the circumferential direction. From Eq. (9) it is clear that for the case $D_1 > 1$ the stress exceeds the allowable stress σ_{allow} at least at one point in I-fc. The scalar D_1 characterizes the *local* stress environment in I-fc and is, therefore, related to the localized vulnerability status of the tissue.

The scalar D_2 in Eq. (8) is defined as

$$D_2 = \frac{\sum_{i=1}^{n_c^{I-fc}} \sigma_i^{I-fc} \Omega_i^*}{\sum_{i=1}^{n_c^{I-fc}} \sigma_{allow} \Omega_i^*} \quad \text{with} \quad \Omega_i^* = \begin{cases} \Omega_i & \text{if } \sigma_i^{I-fc} > \sigma_{allow} \\ 0 & \text{otherwise} \end{cases} \quad (10)$$

where n_c^{I-fc} is the total number of finite elements within the volume of I-fc, and σ_i^{I-fc} denotes the maximum principal Cauchy stress in the finite element i of I-fc. Both stress quantities σ_i^{I-fc} and σ_{allow} are weighted by the volume Ω_i of the finite element i in order to make D_2 mesh independent. The scalar D_2 considers only those finite elements in which the maximum principal stress σ_i^{I-fc} is higher than the allowable stress σ_{allow} . It characterizes the *global* stress environment within I-fc and is, therefore, related to the overall vulnerability status of the tissue. From definitions (8)–(10) one may conclude that lower values of D_1 and D_2 (and consequently ξ) are related to more stable caps, while higher values indicate a higher risk of cap rupture.

4 Results

Here we present the most illustrative results of the numerical analysis, in particular, we focus on the 3D stress fields of the

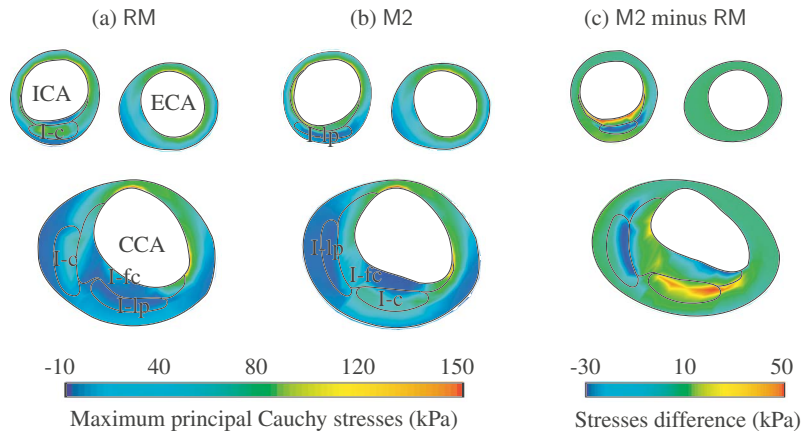


Fig. 4 Maximum principal Cauchy stress at the deformed configuration of the cross sections A, at $z=53.6$ mm, and B, at $z=64.0$ mm (for the geometrical situation see Fig. 2) for (a) model RM ($V_{I-lp}=25\%$, $V_{I-c}=75\%$) and (b) model M2 ($V_{I-lp}=75\%$, $V_{I-c}=25\%$). Stress difference between models M2 and RM at the unloaded configuration of the considered cross sections (c). For the sake of clearness, the boundaries of fibrous cap, lipid core, and calcification are shown.

arterial tissues for the models RM and M2. Next, the stress difference between the two models and the changes in the maximum principal stress for the four models in I-fc are presented. Finally, the changes in the vulnerability index due to morphological variations are documented.

4.1 Predicted Stress Field. Figure 4(a) depicts the distribution of the maximum principal Cauchy stress at the deformed configuration of the characteristic cross sections A and B (Fig. 2) for model RM. Since the circumferential arterial direction is the main loading direction it can be concluded that one principal axis is close to the circumferential direction. A study of Fig. 4(a) reveals that the highest stress regions are located at the thinnest part of W-nos and, most importantly, in the vicinity of the shoulders of I-fc. These results correlate well with the intimal tear sites found at necropsy (see, e.g., Refs. [4,17]) and point out that I-lp is under a relatively low compressive hydrostatic pressure, while in the stiff calcified tissue I-c higher stresses are identified. The presented findings are in agreement with other computational studies [21,22,24].

In Fig. 4(b) the results for model M2 are illustrated. In this model for which I-lp and I-c are interchanged (Table 2), the strain and stress distributions are significantly different. Even though I-c and W-nos bear the main load of the structure, larger areas of maximal stresses are identified in the fibrous cap. This can also be clearly seen in Fig. 4(c), where the stress difference between the models M2 and RM is plotted with respect to the unloaded configuration of the lesion. It should be noted that for the internal carotid artery the stresses inside I-fc for model M2 increase by almost 50 kPa when compared with model RM, characterizing thus a more rupture-prone stenosis.

Figure 5 illustrates the changes in the maximum principal Cauchy stress for the four models in the fibrous cap, which is the most detrimental tissue to plaque stability. In particular, the ranges of stress are plotted with respect to the volume of I-fc. From the figure it is evident that the models M2 and M3 (75% and 100% I-lp, respectively) lead to higher stresses. A positive correlation between the increase in I-lp portion and the mechanical stress in I-fc is evident.

4.2 Predicted Fibrous Cap Vulnerability. According to an experimental study on nine human high-grade stenotic arteries [29], the fibrous cap along the circumferential direction exhibits the lowest fracture stress of all intimal tissues investigated, with a

value of $\sigma_{ult}^{I-fc}=254.8 \pm 79.8$ kPa. Hence, for the present study we used 250 kPa and a value of 5 for the safety factor f_s , which gives an allowable stress σ_{allow} of 50 kPa.

Figure 6 depicts the distribution of the maximum principal Cauchy stress σ^{I-fc} in the finite elements of I-fc for model M2 (75% I-lp). As can be seen, the maximum principal stress is higher than the allowable stress σ_{allow} for several finite elements (compare also with Fig. 5). The stress level at those elements is, therefore, considered to be critical, while the stress level at the other elements is considered to be safe. For the computation of the scalar D_1 , the maximum stress $\max(\sigma^{I-fc})$ at $i=12$, indicated by the symbol \star , is relevant, while every finite element in which the stress is above σ_{allow} contributes to the component D_2 .

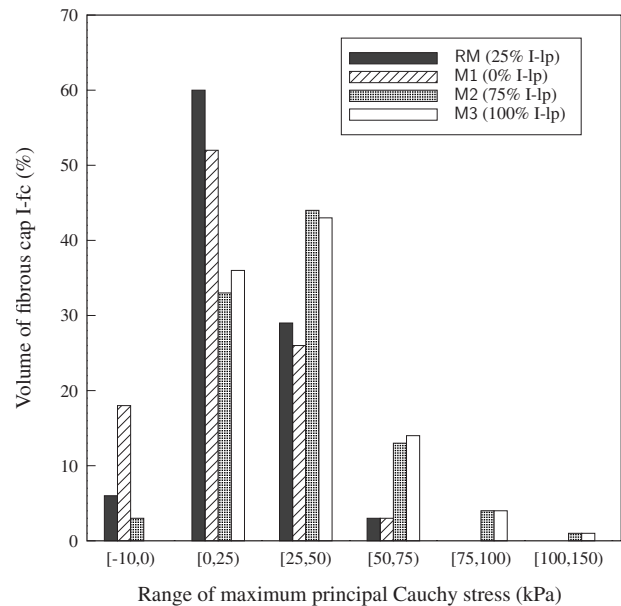


Fig. 5 Maximum principal Cauchy stress in the fibrous cap I-fc for the four models (Table 2). The ranges of stress are plotted with respect to the volume of I-fc. As the tissue composition becomes richer in lipid higher stresses are identified in the fibrous cap.

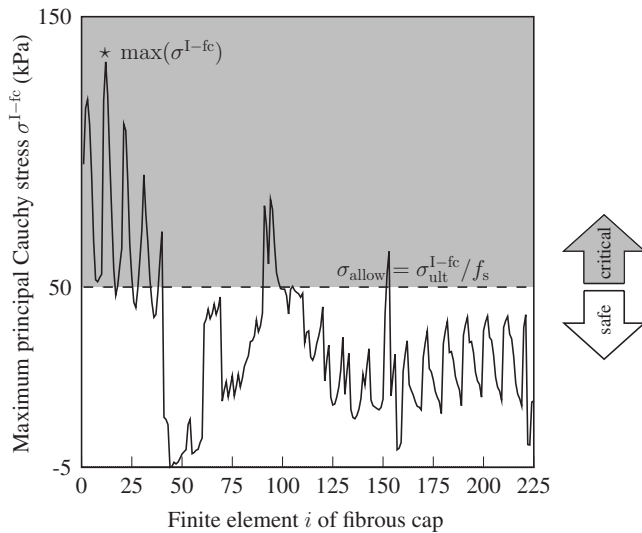


Fig. 6 Maximum principal Cauchy stress σ^{I-fc} in the finite elements of the fibrous cap I-fc for model M2 (75% I-lp). At several locations the stresses in I-fc exceed the allowable stress $\sigma_{allow}=50$ kPa. For scalar D_1 , i.e., Eq. (9), the maximum stress $\max(\sigma^{I-fc})$ at $i=12$ (symbol $*$) is relevant, while for scalar D_2 , i.e., Eq. (10), every finite element in which the stress is above σ_{allow} is considered.

In order to compare the rupture-risk of the four lesion morphologies (RM, M1, M2, and M3), the vulnerability index ξ , as defined in Eq. (8), is computed by assuming equal weighting factors ($w_1=w_2=0.5$). The results are illustrated in Fig. 7 from which it is evident that $\xi > 1$ for all models. With the selected safety factor, the morphologies of all four cases are considered to be vulnerable. The smallest vulnerability index ($\xi=1.57$) is obtained for model M1 for which no I-lp is present. For the reference model RM a slightly higher value ξ is computed. However, when

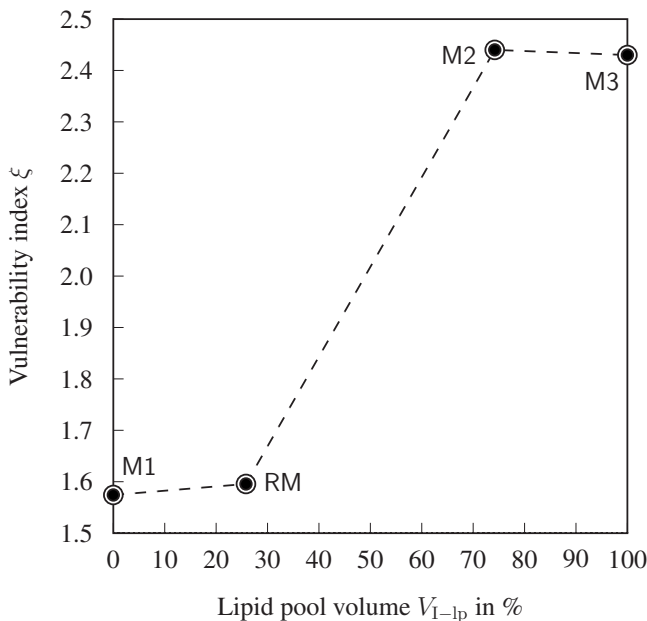


Fig. 7 Vulnerability index ξ , i.e., Eq. (8), for the four models (Table 2) with $w_1=w_2=0.5$. Model M1 has no lipid core while $V_{I-lp}=100\%$ in model M3. For models M2 and M3 the vulnerability index is more than 50% higher in comparison to reference model RM.

the lesion consists of a higher amount of lipid, then the vulnerability index ξ increases considerably (by more than 50%). The lesion composed only by I-lp, i.e., model M3, leads to comparable results to model M2. A heavily loaded fibrous cap is thus detected and, consequently, a higher risk for cap rupture is identified.

5 Discussion and Conclusion

Vulnerable plaque morphology is usually described by gross pathology and intravascular ultrasound. However, morphological criteria alone cannot reliably explain vulnerability, which involves factors such as inflammatory processes, geometry, composition, and wall stresses that occur due to certain loading and boundary conditions, just to mention a few [56]. The last three aspects require biomechanical studies.

Based on the above arguments, we developed an additional multidisciplinary methodology for the quantification of the tissue-specific micromechanical environment of atherosclerotic plaques by combining MR imaging with established mechanical analysis tools. In order to show the methodology, a carotid bifurcation with a high-grade stenosis excised from a human cadaver served as a basis (for MR images see Fig. 1). We generated a highly-resolved 3D geometric model (Fig. 2) using segmentation methods for which both MR and histological images were considered. We segmented four tissues, i.e., nondiseased wall W-nos, fibrous cap I-fc, lipid core I-lp, calcification I-c, and described the nonlinear elastic response of each tissue by a strain-energy function. The material parameters were determined from related extension-inflation tests [34] and from the literature (Table 1). Note that we have not identified the structural arrangement of collagen, and hence the angle φ was used as a phenomenological parameter. Nevertheless, a structural analysis of collagen using methods, such as polarized light microscopy, should be used to obtain related structural parameters; for a recent survey comparing different methods see Ref. [57].

A novel numerical algorithm based on tangential planes was employed to allow the otherwise laborious computation of the local material axes in the case of large 3D arbitrarily curved patient-specific geometric models (Fig. 3). The related algorithm was first described in Ref. [58] focusing on finite element studies of inhomogeneities within the intervertebral disk. To the authors' knowledge, this method has not yet been applied to patient-specific models of arterial tissues. The algorithm provided a robust and fast generation of the 3D collagen fabric; nonuniqueness of the generated fiber directions was not detected even for such a complex geometrical setting of a multilayered bifurcation. In Ref. [59], the problem of identifying local material axes is solved by mapping the undeformed configuration Ω_o of the artery to an eccentric thick-walled tube with configuration $\bar{\Omega}_o$, in which the (local) radial, circumferential, and axial directions can be defined in a straightforward way. A pull-back operation with the rotation tensor provides then the material axes in the initial configuration. Even though this technique seems to address the problem sufficiently, it is demanding and the definition of the configuration $\bar{\Omega}_o$ has an influence on the prediction of the material axes.

In addition to the generated patient-specific geometric model, three variations of the bifurcation's composition were introduced (Table 2). Thereby, we focused on the variation in the I-lp and I-c volumes by keeping the cap thickness constant. The used finite element mesh turned out to be sufficiently fine in all directions. The numerical analysis was performed by considering a blood pressure of 140 mmHg, which is an elevated pressure load. According to Chobanian et al. [60] systolic blood pressure of more than 140 mm Hg is a much more important cardiovascular disease risk-factor than diastolic blood pressure in persons older than 50 years. In addition, data from observational and trial studies suggest that high blood pressure is a main contributor to the profile of atherothrombotic patients [61–63].

The computational analysis of the four models revealed that changes in the volume portion of I-lp lead to significantly different stress distributions in the stenosis. In particular, we identified a correlation between a lipid-rich stenosis and a severely mechanically loaded I-fc prone to rupture (Figs. 4 and 5). Finally, we proposed scalar quantities that are related to the local and global stress environment in I-fc serving as cap vulnerability criteria (Figs. 6 and 7). The introduced (computational) vulnerability index ξ considers a safety factor f_s , which is defined with respect to the ultimate stress of I-fc. Note that there are several ways in which factors of safety can be defined. Higher values of ξ suggest a higher risk of cap rupture. The index ξ provides a more efficient and objective rupture-risk assessment of atherosclerotic plaques. Such a vulnerability index has the potential to bridge the gap between the medical and engineering community and may serve as a more quantitative tool for diagnosis, treatment, and prevention.

Despite some novelties and increased complexities of the used geometric and material models there is room for improvements. The multilayered structure of W-nos was modeled as one homogeneous material, and the material properties of I-fc were assumed to behave similar to the homogenized wall material. Tissue-specific mechanical properties of sclerotic human carotid arteries would improve modeling. In addition, due to the lack of experimental data and computational complexities, residual stresses were not considered in the healthy portion of the bifurcation. Based on the authors' experience there are no (or at least very minor) residual stresses present in the diseased portion of the bifurcation such as the fibrous cap. Consequently, a diseased arterial ring does not spring open when cut in a radial direction within the diseased portion. We did not consider pulsatile blood pressure and fluid-structure interaction models such as presented in Refs. [24,64], which may strengthen the computational findings of our approach. We do know that the stress conditions become critical when the plaque cap becomes very thin, in particular, for mildly stenotic carotid plaques [6]; hence, this parameter should be considered in an upcoming study. The present analysis is limited to the in vitro assessment of rupture-prone plaques. During the last years the ability of in vivo carotid MR imaging has been significantly improved (see, e.g., Refs. [65–68]). 3 T MR scanners are finding their way to the clinical arena, and the development of computerized plaque characterization methods to deal with a large amount of high-resolution multicontrast data is ongoing. The extension of the proposed methodology to in vivo implementation is, therefore, feasible.

In the present study a model of a human carotid bifurcation served as a (test) basis for the developed computational platform. The methodology can also be applied to other arteries such as coronary arteries to evaluate the rupture-risk. One may argue that the results of the presented method-oriented study were highly individual and not representative for atherosclerotic lesions in general. The investigation of only one plaque sample undoubtedly restricts general conclusions, however, the prospect of the documented attempt is the individual diagnosis and assessment of rupture-prone plaques. Moreover, the above discussion suggests that even the study of a single lesion model can simulate novel ideas and provide intriguing insights, which are of general significance for the issue of plaque stability. One should further take into consideration that patient-specific computational analyses have considerable advantages over conventional large clinical trials. For example, they are less expensive and time-consuming, they are harmless to patients, and allow control and systematic variations in all essential parameters.

The combination of MR image data, computerized plaque segmentation and nonlinear finite element analysis, as performed in the present study, constitutes a powerful platform able to investigate quantitatively the biomechanical behavior of atherosclerotic plaques in patient-specific stenoses. This cannot be performed by entirely morphological approaches. In light of the presented re-

sults, the authors feel that the proposed methodology may be of interest to several branches of clinical medicine dealing with vessel diagnosis and therapy including radiology, cardiology, and cardiovascular medicine. The outcome of the current study may serve in vivo patient studies in future.

References

- [1] Allender, St., Scarborough, P., Peto, V., Rayner, M., Leal, J., Luengo-Fernandez, R., and Gray, A., 2008, "European Cardiovascular Disease Statistics, 2008 Edition," British Heart Foundation Health Promotion Research Group and Health Economic Research Centre, Department of Public Health, University of Oxford, www.heartstats.org.
- [2] Rosamond, W., Flegal, K., Furie, K., Go, A., Greenlund, K., Haase, N., Hailpern, S. M., Ho, M., Howard, V., Kissela, B., Kittner, S., Lloyd-Jones, D., McDermott, M., Meigs, J., Moy, C., Nichol, G., O'Donnell, C., Roger, V., Sorlie, P., Steinberger, J., Thom, T., Wilson, M., and Hong, Y., 2008, "Heart Disease and Stroke Statistics—2008 Update," American Heart Association Statistics Committee, and Stroke Statistics Subcommittee, Vol. 117.
- [3] Virmani, R., Burke, A. P., and Farb, A., 1999, "Plaque Rupture and Plaque Erosion," *Thromb. Haemostasis*, **82**, pp. 1–3.
- [4] Davies, M. J., 2000, "The Pathophysiology of Acute Coronary Syndromes," *Heart*, **83**, pp. 361–366.
- [5] Casscells, W., Naghavi, M., and Willerson, J. T., 2003, "Vulnerable Atherosclerotic Plaque: A Multifocal Disease," *Circulation*, **107**, pp. 2072–2075.
- [6] Naghavi, M., Libby, P., Falk, E., Casscells, S. W., Litovsky, S., Rumberger, J., Badimon, J. J., Stefanadis, C., Moreno, P., Pasterkamp, G., Fayad, Z., Stone, P. H., Waxman, S., Raggi, P., Madjid, M., Zarabi, A., Burke, A., Yuan, C., Fitzgerald, P. J., Siscovick, D. S., de Korte, C. L., Aikawa, M., Juhani Airaksinen, E., Assmann, G., Becker, C. R., Chesebro, J. H., Farb, A., Galis, Z. S., Jackson, C., Jang, I. K., Koenig, W., Lodder, R. A., March, K., Demirovic, J., Navab, M., Puri, S. G., Reekher, M. D., Bahr, R., Grundy, S. M., Mehran, R., Colombo, A., Boerwinkle, E., Ballantyne, C., Insull, W., Jr., Schwartz, R. S., Vogel, R., Serruys, P. W., Hansson, G. K., Faxon, D. P., Kaul, S., Drexler, H., Greenland, P., Muller, J. E., Virmani, R., Ridker, P. M., Zipes, D. P., Shah, P. K., and Willerson, J. T., 2003, "From Vulnerable Plaque to Vulnerable Patient: A Call for New Definitions and Risk Assessment Strategies: Part I," *Circulation*, **108**, pp. 1664–1672.
- [7] Falk, E., 1989, "Morphologic Features of Unstable Atherothrombotic Plaques Underlying Acute Coronary Syndromes," *Am. J. Cardiol.*, **63**, pp. 114E–120E.
- [8] Davies, M. J., Richardson, P. D., Woolf, N., Katz, D. R., and Mann, J. J., 1993, "Risk of Thrombosis in Human Atherosclerotic Plaques: Role of Extracellular Lipid, Macrophage, and Smooth Muscle Cell Content," *Br. Heart J.*, **69**, pp. 377–381.
- [9] Moreno, P., Falk, E., Palacios, I., Newell, J. B., Fuster, V., and Fallon, J. T., 1994, "Macrophage Infiltration in Acute Coronary Syndromes. Implications for Plaque Rupture," *Circulation*, **90**, pp. 2775–2778.
- [10] Fayad, Z. A., and Fuster, V., 2001, "Clinical Imaging of the High-Risk or Vulnerable Atherosclerotic Plaque," *Circ. Res.*, **89**, pp. 305–316.
- [11] Yuan, C., Mitsumori, L. M., Beach, K. W., and Maravilla, K. R., 2001, "Carotid Atherosclerotic Plaque: Noninvasive MR Characterization and Identification of Vulnerable Lesions," *Radiology*, **221**, pp. 285–299.
- [12] Yuan, C., Mitsumori, L. M., Ferguson, M. S., Polissar, N. L., Echelard, D., Ortiz, G., Small, R., Davies, J. W., Kerwin, W. S., and Hatsukami, T. S., 2001, "In Vivo Accuracy of Multispectral Magnetic Resonance Imaging for Identifying Lipid-Rich Necrotic Cores and Intraplaque Hemorrhage in Advanced Human Carotid Plaques," *Circulation*, **104**, pp. 2051–2056.
- [13] Trivedi, R. A., U-King-Im, J., Graves, M. J., Horsley, J., Goddard, M., Kirkpatrick, P. J., and Gillard, J. H., 2004, "Multi-Sequence In Vivo MRI Can Quantify Fibrous Cap and Lipid Core Components in Human Carotid Atherosclerotic Plaques," *Eur. J. Vasc. Endovasc. Surg.*, **28**, pp. 207–213.
- [14] Richardson, P. D., Davies, M. J., and Born, G. V. R., 1989, "Influence of Plaque Configuration and Stress Distribution on Fissuring of Coronary Atherosclerotic Plaques," *Lancet*, **334**, pp. 941–944.
- [15] Loree, H. M., Kamm, R. D., Stringfellow, R. G., and Lee, R. T., 1992, "Effects of Fibrous Cap Thickness on Peak Circumferential Stress in Model Atherosclerotic Vessels," *Circ. Res.*, **71**, pp. 850–858.
- [16] Cheng, G. C., Loree, H. M., Kamm, R. D., Fishbein, M. C., and Lee, R. T., 1993, "Distribution of Circumferential Stress in Ruptured and Stable Atherosclerotic Lesions: A Structural Analysis With Histopathological Correlation," *Circulation*, **87**, pp. 1179–1187.
- [17] Burke, A. P., Farb, A., Malcom, G. T., Liang, Y. H., Smialek, J., and Virmani, R., 1997, "Coronary Risk Factors and Plaque Morphology in Men With Coronary Disease Who Died Suddenly," *N. Engl. J. Med.*, **336**(18), pp. 1276–1282.
- [18] Lee, R. T., Schoen, F. J., Loree, H. M., Lark, M. W., and Libby, P., 1996, "Circumferential Stress and Matrix Metalloproteinase 1 in Human Coronary Atherosclerosis. Implications for Plaque Rupture," *Arterioscler., Thromb., Vasc. Biol.*, **16**, pp. 1070–1073.
- [19] Huang, H., Virmani, R., Younis, H., Burke, A. P., Kamm, R. D., and Lee, R. T., 2001, "The Impact of Calcification Upon the Biomechanical Stability of Atherosclerotic Plaques," *Circulation*, **103**, pp. 1051–1056.
- [20] Baldewing, R. A., de Korte, C. L., Schaar, J. A., Mastik, F., and van der Steen, A. F., 2004, "Finite Element Modeling and Intravascular Ultrasound

- Elastography of Vulnerable Plaques: Parameter Variation,” *Ultrasonics*, **42**, pp. 723–729.
- [21] Zheng, J., El Naqa, I., Rowold, F. E., Pilgram, T. K., Woodard, P. K., Saffitz, J. E., and Tang, D., 2005, “Quantitative Assessment of Coronary Artery Plaque Vulnerability by High-Resolution Magnetic Resonance Imaging and Computational Biomechanics: A Pilot Study Ex Vivo,” *Magn. Reson. Med.*, **54**, pp. 1360–1368.
- [22] Li, Z. Y., Howarth, S. P., Trivedi, R. A., U-King-Im, J. M., Graves, M. J., Brown, A., Wang, L., and Gillard, J. H., 2006, “Stress Analysis of Carotid Plaque Rupture Based on In Vivo High Resolution MRI,” *J. Biomech.*, **39**, pp. 2611–2622.
- [23] Versluis, A., Bank, A. J., and Douglas, W. H., 2006, “Fatigue and Plaque Rupture in Myocardial Infarction,” *J. Biomech.*, **39**, pp. 339–347.
- [24] Tang, D., Yang, C., Zheng, J., Woodard, P. K., Saffitz, J. E., Sicard, G. A., Pilgram, T. K., and Yuan, C., 2005, “Quantifying Effects of Plaque Structure and Material Properties on Stress Distributions in Human Atherosclerotic Plaques Using 3D FSI Models,” *ASME J. Biomech. Eng.*, **127**, pp. 1185–1194.
- [25] Li, Z. Y., Howarth, S. P., Tang, T., and Gillard, J. H., 2006, “How Critical Is Fibrous Cap Thickness to Carotid Plaque Stability? A Flow-Plaque Interaction Model,” *Stroke*, **37**, pp. 1195–1199.
- [26] Schulze-Bauer, C. A. J., Regitnig, P., and Holzapfel, G. A., 2002, “Mechanics of the Human Femoral Adventitia Including High-Pressure Response,” *Am. J. Physiol. Heart Circ. Physiol.*, **282**, pp. H2427–H2440.
- [27] Holzapfel, G. A., Sommer, G., Gasser, C. T., and Regitnig, P., 2005, “Determination of the Layer-Specific Mechanical Properties of Human Coronary Arteries With Non-Atherosclerotic Intimal Thickening, and Related Constitutive Modelling,” *Am. J. Physiol. Heart Circ. Physiol.*, **289**, pp. H2048–H2058.
- [28] Holzapfel, G. A., Schulze-Bauer, C. A. J., and Stadler, M., 2000, “Mechanics of Angioplasty: Wall, Balloon and Stent,” *Mechanics in Biology*, J. Casey and G. Bao, eds., American Society of Mechanical Engineers (ASME), New York, AMD-Vol. 242/BED-Vol. 46, pp. 141–156.
- [29] Holzapfel, G. A., Sommer, G., and Regitnig, P., 2004, “Anisotropic Mechanical Properties of Tissue Components in Human Atherosclerotic Plaques,” *ASME J. Biomech. Eng.*, **126**, pp. 657–665.
- [30] Holzapfel, G. A., Stadler, M., and Schulze-Bauer, C. A. J., 2002, “A Layer-Specific Three-Dimensional Model for the Simulation of Balloon Angioplasty Using Magnetic Resonance Imaging and Mechanical Testing,” *Ann. Biomed. Eng.*, **30**, pp. 753–767.
- [31] Beaussier, H., Masson, I., Collin, C., Bozec, E., Laloux, B., Calvet, D., Zidi, M., Boutouyrie, P., and Laurent, S., 2008, “Carotid Plaque, Arterial Stiffness Gradient, and Remodeling in Hypertension,” *Hypertension*, **52**, pp. 729–736.
- [32] Davies, M. J., 2001, “Going From Immutable to Mutable Atherosclerotic Plaques,” *Am. J. Cardiol.*, **88**, pp. 2F–9F.
- [33] Fuster, V., Moreno, P. R., Fayad, Z. A., Corti, R., and Badimon, J. J., 2005, “Atherothrombosis and High-Risk Plaque: Part I: Evolving Concepts,” *J. Am. Coll. Cardiol.*, **46**, pp. 937–954.
- [34] Sommer, G., Regitnig, P., Koeltringer, L., and Holzapfel, G. A., 2009, “Biaxial Mechanical Properties of Intact and Layer-Dissected Human Carotid Arteries at Physiological and Supra-Physiological Loadings,” submitted.
- [35] Sary, H. C., 2003, *Atlas of Atherosclerosis: Progression and Regression*, 2nd ed., The Parthenon, Boca Raton, FL.
- [36] Auer, M., Stollberger, R., Regitnig, P., Ebner, F., and Holzapfel, G. A., 2006, “3-D Reconstruction of Tissue Components for Atherosclerotic Human Arteries Based on High-Resolution MRI,” *IEEE Trans. Med. Imaging*, **25**, pp. 345–357.
- [37] Piegel, L. A., and Tiller, W., 1997, *The NURBS Book*, 2nd ed., Springer-Verlag, New York.
- [38] R. McNeel and Associates, 2005, “Rhinoceros—NURBS Modeling for Windows, Version 3.0 User’s Guide,” Seattle, WA.
- [39] Humphrey, J. D., 2002, *Cardiovascular Solid Mechanics. Cells, Tissues, and Organs*, Springer-Verlag, New York.
- [40] G. A. Holzapfel, and R. W. Ogden, eds., 2006, *Mechanics of Biological Tissue*, Springer-Verlag, Heidelberg.
- [41] G. A. Holzapfel, and R. W. Ogden, eds., 2009, *Biomechanical Modelling at the Molecular, Cellular and Tissue Levels*, Springer-Verlag, Wien, NY.
- [42] Holzapfel, G. A., Stadler, M., and Gasser, T. C., 2005, “Changes in the Mechanical Environment of Stenotic Arteries During Interaction With Stents: Computational Assessment of Parametric Stent Design,” *ASME J. Biomech. Eng.*, **127**, pp. 166–180.
- [43] Holzapfel, G. A., Gasser, T. C., and Ogden, R. W., 2000, “A New Constitutive Framework for Arterial Wall Mechanics and a Comparative Study of Material Models,” *J. Elast.*, **61**, pp. 1–48.
- [44] Holzapfel, G. A., and Gasser, T. C., 2001, “A Viscoelastic Model for Fiber-Reinforced Composites at Finite Strains,” *Comput. Methods Appl. Mech. Eng.*, **190**, pp. 4379–4403.
- [45] Holzapfel, G. A., and Weizsäcker, H. W., 1998, “Biomechanical Behavior of the Arterial Wall and Its Numerical Characterization,” *Comput. Biol. Med.*, **28**, pp. 377–392.
- [46] Gundiah, N., Ratcliffe, M. B., and Pruitt, L. A., 2007, “Determination of Strain Energy Function for Arterial Elastin: Experiments Using Histology and Mechanical Tests,” *J. Biomech.*, **40**, pp. 586–594.
- [47] Holzapfel, G. A., 2000, *Nonlinear Solid Mechanics. A Continuum Approach for Engineering*, Wiley, Chichester, West Sussex, UK.
- [48] Holzapfel, G. A., Gasser, T. C., and Ogden, R. W., 2004, “Comparison of a Multi-Layer Structural Model for Arterial Walls With a Fung-Type Model, and Issues of Material Stability,” *ASME J. Biomech. Eng.*, **126**, pp. 264–275.
- [49] Demiray, H., 1972, “A Note on the Elasticity of Soft Biological Tissues,” *J. Biomech.*, **5**, pp. 309–311.
- [50] Kioussis, D. E., Gasser, T. C., and Holzapfel, G. A., 2007, “A Numerical Model to Study the Interaction of Vascular Stents With Human Atherosclerotic Lesions,” *Ann. Biomed. Eng.*, **35**, pp. 1857–1869.
- [51] CUBIT Team, 2005, “CUBIT 10.0 User’s Manual,” Sandia National Laboratories, Albuquerque, NM.
- [52] Taylor, R. L., 2005, “FEAP—A Finite Element Analysis Program, Version 7.5 User Manual,” University of California at Berkeley, Berkeley, CA.
- [53] Schulze-Bauer, C. A. J., Mörth, C., and Holzapfel, G. A., 2003, “Passive Biaxial Mechanical Response of Aged Human Iliac Arteries,” *ASME J. Biomech. Eng.*, **125**, pp. 395–406.
- [54] Fridez, P., Zulliger, M., Bobard, F., Montorzi, G., Miyazaki, H., Hayashi, K., and Stergiopoulos, N., 2003, “Geometrical, Functional, and Histomorphometric Adaptation of Rat Carotid Artery in Induced Hypertension,” *J. Biomech.*, **36**, pp. 671–680.
- [55] Tang, D., Yang, C., Zheng, J., Woodard, P. K., Saffitz, J. E., Petrucci, J. D., Sicard, G. A., and Yuan, C., 2005, “Local Maximal Stress Hypothesis and Computational Plaque Vulnerability Index for Atherosclerotic Plaque Assessment,” *Ann. Biomed. Eng.*, **33**, pp. 1789–1801.
- [56] Finet, G., Ohayon, J., Rioufol, G., Lefloch, S., Tracqui, P., Dubreuil, O., and Tabib, A., 2007, “Morphological and Biomechanical Aspects of Vulnerable Coronary Plaque,” *Arch. Mal Coeur Vaiss.*, **100**, pp. 547–553.
- [57] Holzapfel, G. A., 2008, “Collagen in Arterial Walls: Biomechanical Aspects,” *Collagen. Structure and Mechanics*, P. Fratzl, ed., Springer-Verlag, Heidelberg, pp. 285–324.
- [58] Karajan, N., Ehlers, W., Markert, B., Acartürk, A., and Wieners, C., 2005, “FE Treatment of Inhomogeneities Within the Intervertebral Disc,” *Appl. Math. Mech.*, **5**, pp. 237–238.
- [59] Gasser, T. C., and Holzapfel, G. A., 2007, “Modeling Plaque Fissuring and Dissection During Balloon Angioplasty Intervention,” *Ann. Biomed. Eng.*, **35**, pp. 711–723.
- [60] Chobanian, A. V., Bakris, G. L., Black, H. R., Cushman, W. C., Green, L. A., Izzo, J. L., Jones, D. W., Materson, B. J., Oparil, S., Wright, J. T., and Roccella, E. J., 2003, “The Seventh Report of the Joint National Committee on Prevention, Detection, Evaluation and Treatment of High Blood Pressure,” *JAMA, J. Am. Med. Assoc.*, **289**, pp. 2560–2572.
- [61] Franklin, S. S., Larson, M. G., Khan, S. A., Wong, N. D., Leip, E. P., Kannel, W. B., and Levy, D., 2001, “Does the Relation of Blood Pressure to Coronary Heart Disease Risk Change With Aging? The Framingham Heart Study,” *Circulation*, **103**, pp. 1245–1249.
- [62] Bhatt, D. L., Steg, P. G., Ohman, E. M., Hirsch, A. T., Ikeda, Y., Mas, J. L., Goto, S., Liao, C. S., Richard, A. J., Röther, J., and Wilson, P. W., and REACH Registry Investigators, 2006, “International Prevalence, Recognition, and Treatment of Cardiovascular Risk Factors in Outpatients With Atherothrombosis,” *JAMA, J. Am. Med. Assoc.*, **295**, pp. 180–189.
- [63] Ohman, E. M., Bhatt, D. L., Steg, P. G., Goto, S., Hirsch, A. T., Liao, C. S., Mas, J. L., Richard, A. J., Röther, J., Wilson, P. W., and REACH Registry Investigators, 2006, “The Reduction of Atherothrombosis for Continued Health (REACH) Registry: An International, Prospective, Observational Investigation in Subjects at Risk for Atherothrombotic Events-Study Design,” *Am. Heart J.*, **151**, pp. 786.e1–786.e10.
- [64] Kaazempur-Mofrad, M. R., Isasi, A. G., Younis, H. F., Chan, R. C., Hinton, D. P., Sukhova, G., LaMuraglia, G. M., Lee, R. T., and Kamm, R. D., 2004, “Characterization of the Atherosclerotic Carotid Bifurcation Using MRI, Finite Element Modeling, and Histology,” *Ann. Biomed. Eng.*, **32**, pp. 932–946.
- [65] Toussaint, J. F., LaMuraglia, G. M., Southern, J. F., Fuster, V., and Kantor, H. L., 1996, “Magnetic Resonance Images Lipid, Fibrous, Calcified, Hemorrhagic, and Thrombotic Components of Human Atherosclerosis *In Vivo*,” *Circulation*, **94**, pp. 932–938.
- [66] Shinnar, M., Fallon, J. T., Wehrli, S., Levin, M., Dalmacy, D., Fayad, Z. A., Badimon, J. J., Harrington, M., Harrington, E., and Fuster, V., 1999, “The Diagnostic Accuracy of Ex Vivo MRI for Human Atherosclerotic Plaque Characterization,” *Arterioscler., Thromb., Vasc. Biol.*, **19**, pp. 2756–2761.
- [67] Hatsukami, T. S., Ross, R., and Yuan, C., 2000, “Visualization of Fibrous Cap Thickness and Rupture in Human Atherosclerotic Carotid Plaque In-Vivo With High Resolution Magnetic Resonance Imaging,” *Circulation*, **102**, pp. 959–964.
- [68] Rogers, W. J., Prichard, J. W., Hu, Y. L., Olson, P. R., Benckart, D. H., Kramer, C. M., Vido, D. A., and Reichel, N., 2000, “Characterization of Signal Properties in Atherosclerotic Plaque Components by Intravascular MRI,” *Arterioscler., Thromb., Vasc. Biol.*, **20**, pp. 1824–1830.